CHALMERS
UNIVERSITY OF TECHNOLOGY

Residual stress determination by neutron diffraction in powder bed fusion-built Alloy 718: Influence of process parameters and post-treatment

Materials and Design 195 (2020) 109045

Contents lists available at ScienceDirect

Materials and Design

journal homepage: www.elsevier.com/locate/matdes

Residual stress determination by neutron diffraction in powder bed fusion-built Alloy 718: Influence of process parameters and post-treatment

S. Goel [a,*], M. Neikter [a], J. Capek [b], E. Polatidis [b], M.H. Colliander [c], S. Joshi [a], R. Pederson [a]

[a] University West, 46186 Trollhättan, Sweden
[b] Laboratory for Neutron Scattering and Imaging, Paul Scherrer Institute, CH-5232 Villigen PSI, Switzerland
[c] Chalmers University of Technology, 41296 Gothenburg, Sweden

HIGHLIGHTS

- Residual stresses determined using calculated and measured stress-free lattice spacings were distinctly different.
- Effect of build orientation on residual stress states in EB-PBF and LPBF found to be an important determinant.
- Difference in residual stresses between EB-PBF and LPBF materials established to be significant.
- LPBF process parameters demonstrated to influence residual stresses in the material.

GRAPHICAL ABSTRACT

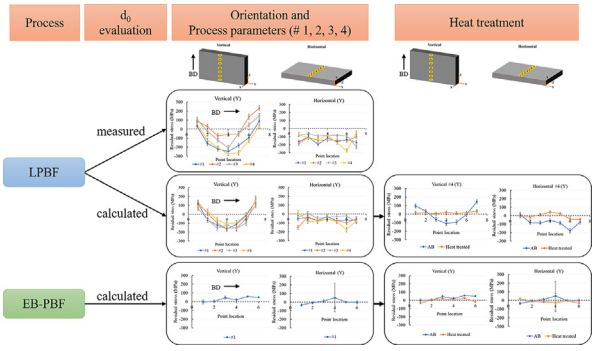

ARTICLE INFO

Article history:
Received 9 June 2020
Received in revised form 29 July 2020
Accepted 5 August 2020
Available online 07 August 2020

Keywords:
Residual stresses
Alloy 718
Neutron diffraction
Laser powder bed fusion (LPBF)
Electron beam powder bed fusion (EB-PBF)
Post-treatment

ABSTRACT

Alloy 718 is a nickel-based superalloy that is widely used as a structural material for high-temperature applications. One concern that arises when Alloy 718 is manufactured using powder bed fusion (PBF) is that residual stresses appear due to the high thermal gradients. These residual stresses can be detrimental as they can degrade mechanical properties and distort components. In this work, residual stresses in PBF built Alloy 718, using both electron and laser energy sources, were measured by neutron diffraction. The effects of process parameters and thermal post-treatments were studied. The results show that thermal post-treatments effectively reduce the residual stresses present in the material. Moreover, the material built with laser based PBF showed a higher residual stress compared to the material built with electron-beam based PBF. The scanning strategy with the lower amount of residual stresses in case of laser based PBF was the chessboard strategy compared to the bi-directional raster strategy. In addition, the influence of measured and calculated lattice spacing (d_0) on the evaluated residual stresses was investigated.

1. Introduction

Alloy 718 is a nickel-based superalloy which exhibits good strength and creep properties and is used as a structural material for high-temperature applications, such as in gas turbines, at temperatures exceeding 600 °C [1,2]. There is a lot of interest in producing Alloy 718

* Corresponding author.
E-mail address: sneha.goel@hv.se (S. Goel).

https://doi.org/10.1016/j.matdes.2020.109045

by additive manufacturing (AM), which is a manufacturing process that melts material layer upon layer according to a predefined design for near-net-shape part fabrication [3,4]. There are numerous benefits associated with AM such as low buy-to-fly ratio and the possibility to manufacture complex structures [3,5,6]. Nonetheless, there are some concerns with defects [7], columnar morphology [8,9], texture [10], leading to anisotropic mechanical behavior. In addition, residual stresses can be present in both laser- and electron-beam based powder bed fusion. In the laser powder bed fusion (LPBF) process, there are large thermal gradients due to the relatively cold build platform. Thus, the resulting fast cooling rates in LPBF lead to the formation of a finer microstructure and hence to an increased strength of the material. Nonetheless, in association with the higher cooling rates for LPBF, compared to the electron beam powder bed fusion (EB-PBF) process [11,12], higher residual stresses form in the material [13]. It should be mentioned that the cooling rates are typically higher in LPBF compared to EB-PBF because of the preheated base plate and use of preheating step before melting in case of the latter [13].

Residual stresses are formed from temperature variations during materials processing such as welding and AM. Additive manufacturing typically involves complex thermal cycling, and the residual stresses build up at a micro level, i.e. for each added layer, which leads to the development of macro residual stresses in finished components [13,14]. The residual stresses, particularly tensile residual stresses in the material, are undesirable, as they can deteriorate the fatigue and tensile properties [15], and make the material prone to cracking, delamination and distortion.

The process parameters used during AM have been found to influence the residual stresses in the built material [14,16–19]. Ali et al. [17] investigated the effects of scanning strategy (scan vector lengths and scan vector rotation) and re-scanning strategy on the residual stresses in LPPF built Ti-6Al-4V and showed that 90° alternating scanning strategy resulted in the lowest residual stresses. This result was also in accordance with the findings of Robinson et al. [16] who showed that in LPBF manufactured Ti using unidirectional vectors, the residual stress was primarily oriented in the scanning direction. Mercilis et al. [18] showed that LPBF built 316L constituted of two residual stress regions, i.e., high tensile residual stresses at the top and bottom (close to the build plate), whereas in the middle, intermediate compressive stresses formed. Mercelis et al. [18] also found that the parameters that were the most important for determining the magnitude and nature (tensile or compressive) of the residual stresses were the material properties, the height of the sample, and the AM process parameters such as laser scanning strategy. Kruth et al. [14] concluded that short scan vectors and preheating of build plate are two parameters that reduce residual stresses. Moreover, it is possible to reduce the residual stresses to certain extent by optimizing the orientation of scan vectors. Another approach to reduce the residual stresses is by exposing the material to thermal post-treatments. Vilaro et al. [20] have shown relief in residual stresses in LPBF built nickel-based superalloy (Nimonic 263) after subjecting the material to annealing treatment.

Neutron diffraction [12,21,22] is a key method for characterizing type-I residual stresses which "equilibrate over macroscopic dimensions" [23,24]. Crystal lattice distortions, i.e. deviations from reference "stress-free" samples, can be measured nondestructively even in relatively thick samples due to the high penetration depth of neutrons [25]. If the lattice spacing (d) in the material is larger than the reference lattice spacing, tensile residual stresses are present, and vice-versa for compressive residual stresses. Therefore, by measuring d-spacing through neutron diffraction and comparing it to a "stress-free" lattice spacing (d_0), the strain (ε) in the material can be calculated. The stress-free lattice spacing is measured in reference samples which can be produced by several methods as described in [26], or can be estimated through certain assumptions and calculations [27]. By determining the stress-free lattice spacing from diffraction measurements, it is possible to eliminate the complication of disentangling the stress-free lattice spacing changes originating from compositional inhomogeneities and residual stresses, which is a common challenge for residual stress analysis in AM [27]. It should be mentioned that accurate determination of stress-free lattice spacing, d_0, is an important concern for residual stress determination using diffraction-based techniques [26]. Notwithstanding the above, comparison of the use of different methods for d_0 determination has not been well understood. In this context it is worth mentioning other methods also exist for residual stress measurements such as, contour method, X-ray diffraction etc. However due to the destructive nature of testing in case of contour method and the limited penetration in case of X-ray diffraction, neutron diffraction for non-destructive evaluation of bulk residual stress is a promising technique [28,29]. Moreover, since the residual stresses are calculated from the strain in the lattice, the measurements are not significantly affected by the material properties, e.g., hardness and extent of cold work [11].

The objective of the study was to investigate the effect of LPBF process parameters such as, scan strategy, laser power and scan speed, on the residual stresses in the fabricated Alloy 718 material. Moreover, the influence of build orientation on residual stress was also studied. The residual stresses in the LPBF Alloy 718 were also compared with EB-PBF material. In addition, two approaches for determination of stress-free lattice spacing have been compared. The same samples tested in as-built condition, for both LPBF and EB-PBF, were also subsequently subjected to annealing treatment to evaluate the residual stress reduction. Understanding the residual stresses and how to relieve them are crucial for future applications of LPBF and EB-PBF built Alloy 718, and although similar studies have been published e.g. [12,30,31], no comprehensive study has been undertaken addressing the effect of processing parameters and post-treatments on the development of residual stresses.

2. Experimental procedure

2.1. Sample fabrication of LPBF and EB-PBF built Alloy 718

The LPBF built Alloy 718 samples used in the present study were provided by GKN Aerospace AB (Filton, UK). The specimens were produced using an EOS M290 machine. The nominal chemical composition of the inert gas atomized Alloy 718 powder used is given in Table 1; both the nitrogen and oxygen contents were below ~300 ppm. Four sets of wall samples, each sample with dimensions 100x50x6 mm^3, were produced with different processing parameters, and only the process parameters that were altered are stated in Table 2. Each set of samples comprised a pair of a vertical and a horizontal wall specimen as shown in Fig. 1. All the builds were fabricated using a layer thickness of 40 μm and a hatch distance of 110 μm. It should be mentioned that the sample set #1 was built using the default machine settings. After fabrication, all the samples were removed from the build plate using electric discharge machining.

One set (vertical and horizontal samples) of EB-PBF specimens was manufactured using an Arcam A2X machine, at University West, Sweden. The feedstock powder used, Sandvik Osprey® Alloy718, was manufactured using vacuum induction melting and subsequent inert gas atomization with argon gas. The resulting chemical composition is displayed in Table 1; both the nitrogen and oxygen contents were below 250 ppm. The powder was processed using the typical recommended Arcam settings [32]. The powder layer thickness used was

Table 1
Nominal chemical composition of Alloy 718 powder used to produce the LPBF and EB-PBF samples.

Process	Element	Ni	Cr	Fe	Nb	Mo	Ti	Al
LPBF	Wt%	Bal.	19.2	18.5	5.3	3.1	1.0	0.6
EB-PBF	Wt%	Bal.	18.7	18.0	5.1	3.0	0.9	0.4

Table 2
The process parameters varied to produce the four LPBF sample sets.

Sample set	Laser power (W)	Scan speed (mm/s)	Scanning strategy
#1	285	960	Bi-directional Raster
#2	340	1145	Bi-directional Raster
#3	340	960	Bi-directional Raster
#4	285	960	Chessboard (67° rotation)

75 μm and the hatch distance was set to 125 μm. It should be mentioned that the powder layer thickness is the distance by which the build platform is lowered for processing of each subsequent layer. For melting, bi-directional raster strategy was used.

2.2. Neutron diffraction measurements

Neutron diffraction experiments were performed on the time-of-flight POLDI diffractometer at the Swiss Spallation Source, at PSI, Switzerland. All the samples tested in as-built condition were re-tested after applying annealing treatment (specified later in Section 2.3). The {311} diffraction peak was used for strain evaluation because, in face centred cubic (FCC) Ni-based alloys such as Alloy 718, it is the least affected by the intragranular strain and inter-phase strains [33–35] and the plane-specific elastic properties are similar to those of the bulk to accurately reflect macroscopic stress in the material. For data collection, seven equally spaced points (for LPBF, whereas for EB-PBF six equally spaced points) were chosen along the width of the specimens as shown in Fig. 1. For each point, a gauge volume of $3.8 \times 3.8 \times 3.8\ mm^3$ was defined by two pairs of diaphragms perpendicular to the incident beam direction; Fig. 2 shows a schematic of the setup. This together with a radial collimator for the diffracted beam, resulted in a satisfactory trade-off between spatial resolution and counting time for this study. The gauge volume was aligned and fully submerged in the material to avoid "pseudo- strains" due to partial gauge volume burial. All the points were undertaken with the center of the gauge volume being at the center of the wall thickness, i.e. at X = 3 mm. The obtained data were fitted using Mantid [36] and the fitted results were processed using in-house MATLAB scripts.

2.3. Annealing treatment and stress-free reference

The same samples that were measured in the as-built condition were annealed for 2 h at 1066 °C, which is a typical homogenization treatment [37] and has been also adapted for stress relief of AM processed Alloy 718 [38]. The residual stresses in all annealed samples were measured at the same locations for direct comparison with the as-built samples. After determination of the *d*-spacing in the annealed samples, the sample for d_0 measurement was sectioned out as a thin strip from the vertical LPBF sample #4 (see Fig. 3 (a)). Furthermore, around the measurement points, comb-type cuts were made to further relieve the stresses in order to ensure that strain relaxes in the d_0 sample, as previously reported [33]. The reference d_0 measurement was undertaken at three points along the build direction as illustrated in Fig. 3 (a) to investigate possible variations due to microstructural or chemical heterogeneity. This has been reported to be an important aspect while measuring lattice spacing in AM manufactured material [33]. However, in the present study and within the experimental accuracy, it was seen that the variation is not so significant, i.e. in X and Z directions the standard deviation from the mean value is smaller than the experimental error, which corresponds to a strain uncertainty of only 35 με (see Fig. 3 (b)).

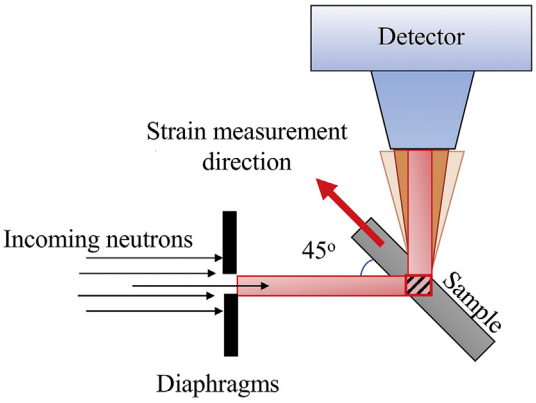

Fig. 2. Schematic of the measurement setup at POLDI.

2.4. Neutron diffraction data analysis

For LPBF samples, the measured interplanar spacing d_0^{311} was determined using an average of values evaluated from the three measurement points (bottom, middle, top) as shown in Fig. 3 (a). No significant variation in d_0 was observed at the three locations. Therefore, an average value of 1.08613 Å was used for d_0^{311} measured as shown in Fig. 3 (b). Thereafter, the lattice strain was determined using the interplanar spacing, d^{311}, as follows:

$$\varepsilon_{ii}^{311} = \frac{d_{ii}^{311} - d_0^{311}}{d_0^{311}} \quad (1)$$

where i = X, Y, Z represents the three orthogonal directions. Using the above residual strain measured in three orthogonal directions and the

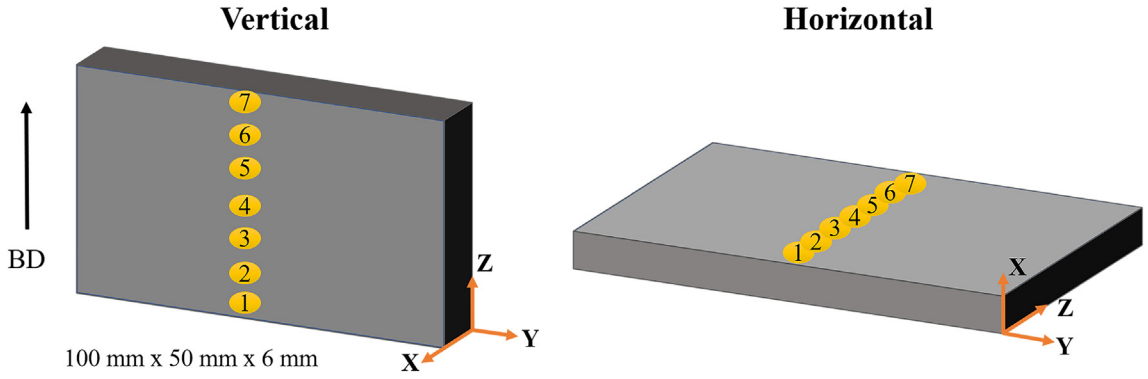

Fig. 1. Schematic of the vertical and horizontal wall samples showing the location of the measurement points (1 to 7). The arrow indicates the build direction (BD) and the coordinate axes correspond to the strain/stress measurement coordination system.

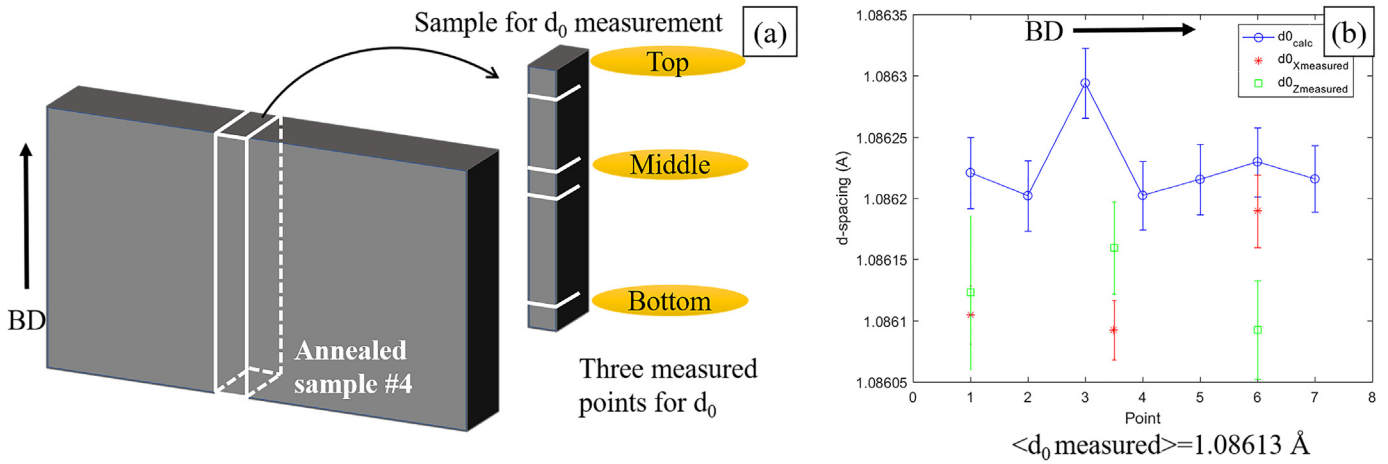

Fig. 3. Schematic showing sample extraction from an annealed vertical LPBF specimen #4 for d_0 determination and the three measurement points (a). The measured (experimental) and calculated d_0 in vertical sample #4 (b). The build direction is indicated by the arrow on the left.

generalized Hooke's law, the residual stresses in the corresponding directions were evaluated as follows:

$$\begin{pmatrix}\sigma_{XX}\\ \sigma_{YY}\\ \sigma_{ZZ}\end{pmatrix} = \frac{E}{(1+\nu)(1-2\nu)}\begin{pmatrix}1-\nu & \nu & \nu\\ \nu & 1-\nu & \nu\\ \nu & \nu & 1-\nu\end{pmatrix}\begin{pmatrix}\varepsilon_{XX}\\ \varepsilon_{YY}\\ \varepsilon_{ZZ}\end{pmatrix} \quad (2)$$

where E is the Young's modulus and ν is the Poisson's ratio. The values of E and ν corresponding to {311} lattice planes used were 200 GPa and 0.3, after [39]. When thin walls are built [28], we can assume a plane stress state, i.e. $\sigma_{XX} = 0$ and measuring a refence d_0 value is no longer required as previously done in [27]. Thus, d_0 can be calculated for each measurement point as follows:

$$d_0^{311} = \frac{d_{XX}^{311} + \nu\left(-d_{XX}^{311} + d_{YY}^{311} + d_{ZZ}^{311}\right)}{1+\nu} \quad (3)$$

and the σ_{YY} and σ_{ZZ} can be calculated by the following equation:

$$\sigma_{ii} = \frac{\left(d_{XX}^{311} - d_{ii}^{311}\right)E}{d_{XX}^{311}(\nu-1) - \left(d_{ii}^{311} + d_{jj}^{311}\right)\nu} \quad (4)$$

where i and j can be either Y or Z. An example of calculated d_0^{311} is shown in Fig. 3 (b) for sample #4. Point 3 seems to be an outlier, however this only corresponds to 85 με which does not affect the lattice strain calculation significantly. The EB-PBF samples exhibit strong crystallographic texture. A consequence of strong texture is that the {311} diffraction peak does not appear in all directions for obtaining all the strain components. Time-of-flight diffraction at POLDI is particularly valuable since all reflections, permitted by the texture, are captured simultaneously and hence for EB-PBF, the {200} diffraction peak is used. The values of E and ν corresponding to {200} lattice planes used were 165 GPa and 0.3, after [39].

2.5. Electron backscattered diffraction - EBSD

Sections of the selected annealed vertical samples were extracted using alumina cutting blade, and sections along the build direction (BD) were hot mounted. All these samples were taken from a region close to the mid-height of the wall samples. The samples were then ground and polished, with a final polish using 0.05 μm silica suspension. For electron backscattered diffraction (EBSD) analysis, a field emission gun scanning electron microscope (FEG SEM) Zeiss ULTRA 55 equipped

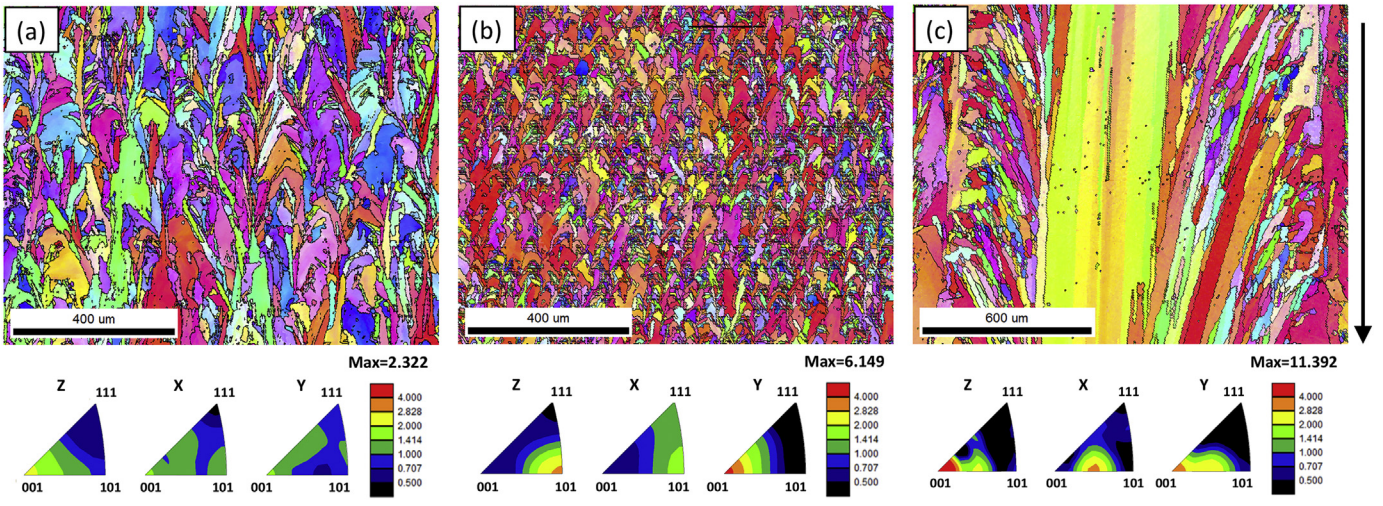

Fig. 4. Orientation map with Inverse Pole Figure (IPF) coloring in the Y-direction (long direction of the wall) and IPF triangles showing the dominant texture components along the 3 principal directions X, Y and Z for the vertical (a) LPBF sample #1, (b) LPBF sample #4 and (a) EB-PBF sample. The arrow shows the building direction for all samples.

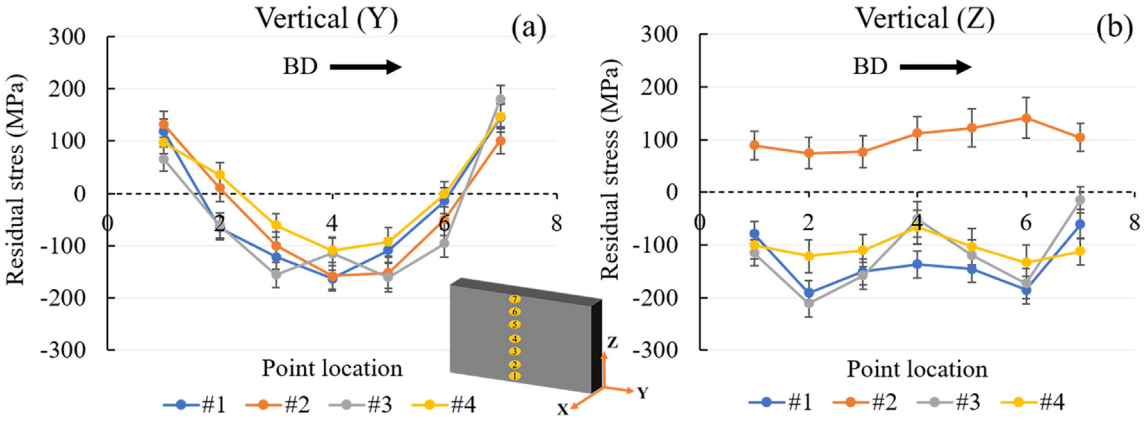

Fig. 5. Residual stresses along (a) Y and (b) Z directions for all the as-built LPBF vertical samples evaluated using Eqs. (3) and (4), the through thickness stress (along X) is assumed to be zero. The arrow indicates the build direction.

with EDAX Hikari Camera operated at 20 kV in high current mode with 120 μm aperture was used. The EBSD raw data was post-processed using the EDAX OIM Analysis 7.3 software.

3. Results

3.1. Microstructure and crystallographic texture comparison: LPBF and EB-PBF

The manufacturing processes as well as the scanning strategy greatly influence the microstructure as shown in Fig. 4 for vertical samples. EB-PBF resulted in heterogeneous microstructure with one large grain in the middle that is about 400 μm wide and longer than the field of view of the EBDS map (1.2 mm). Large elongated grains aligned with the building direction surround this grain. Whereas, the microstructure of the LPBF samples appears to be more homogeneous, and the chessboard scanning strategy resulted in the smallest grain size (Fig. 4 (b)); i.e. 25 μm (sample #4) compared to the 58 μm (sample #1) in sample produced by bi-directional raster scanning strategy. Moreover, the crystallographic texture is significantly different between these two samples. The bi-directional raster scanning strategy in LPBF sample #1 resulted in relatively mild ⟨100⟩ texture in BD and nearly random in X-Y plane (Fig. 4 (a)). The chessboard scanning strategy in LPBF sample #4 caused relatively strong ⟨101⟩ texture along the building direction (Z) and relatively strong <100> along the in-plane direction (Y) (Fig. 4 (b)). Finally, the EB-PBF results in significantly strong <100> texture along the building direction and relatively strong near <100> texture along the in-plane directions (X and Y), mainly dominated by the very large grains in the center of the sample which reside in the middle of the neutron gauge volume (Fig. 4 (c)). The latter strong texture affects the choice of diffraction peak for residual strain calculation and it is further discussed in Section 4.2. These findings agree well with the neutron diffraction patterns obtained for all the directions measured for residual stress calculation.

3.2. As-built LPBF Alloy 718: calculated d_0 from plane stress assumption

The residual stress values from the {311} lattice planes, evaluated using the calculated d_0 (Eq. (3)), in the as-built condition for the vertical samples are given in Fig. 5, wherein the error bars represent the error propagation in determining the peak positions (by peak fitting). The evolution of residual stress σ_{YY}, with build height followed a 'U-shaped' pattern. From the bottom of the build to the top, the nature of the stress varied from tensile to compression and then tensile again as shown in Fig. 5 (a). Comparing residual stress, σ_{YY}, in specimen #1 and #4, which were produced with raster and chessboard strategy, respectively, revealed the latter to contain slightly lower residual stress. The nature of residual stress along the z-direction was relatively invariable for a given sample as shown in Fig. 5 (b). The residual stresses σ_{ZZ} in the specimens #1, #3, #4 were compressive in nature whereas tensile in sample #2. The only parameter that is different between samples #2 and #3 is the laser scanning speed, which could have caused variation in cooling rate, thereby affecting development of residual stresses in the material. A study on LPBF built Alloy 718 has shown increase in scan speed to result in faster cooling rates [40]. The value of σ_{ZZ} for specimen #4 was lower than for #1. By comparing results for samples #1 and #3 there is no observed effect of increased laser power, i.e., increase in energy input, on the residual stress. Residual stresses in the corresponding

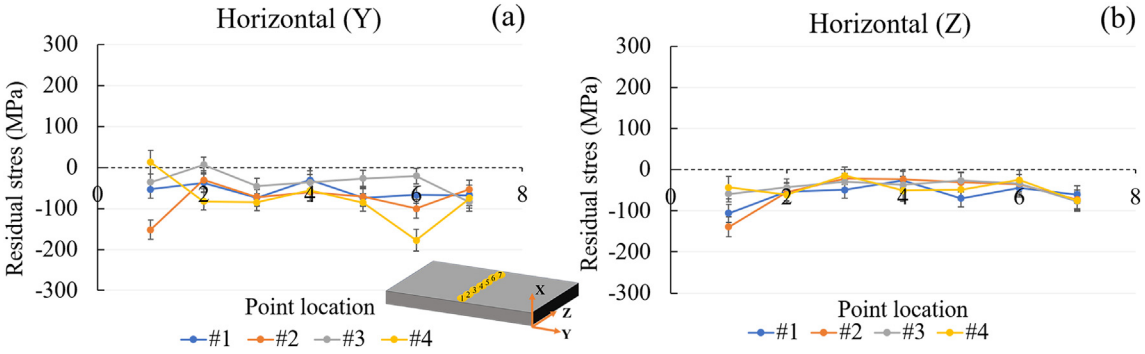

Fig. 6. Residual stresses along (a) Y and (b) Z directions for all the as-built LPBF horizontal samples evaluated using Eqs. (3) and (4); the through thickness stress (along X) is assumed to be zero. All the points were measured at the same build height.

horizontal samples were much lower than in the vertical samples as shown in Fig. 6. It should be noted that the residual stresses appear compressive in both Y and Z directions, while direction X is assumed to be zero, which does not satisfy the stress equilibrium. This is due to the choice of d_0. For the plane stress assumption, the stress in the direction X is assumed zero. The direction X corresponds to the building direction of the horizontal samples, while residual stresses are seen to be high along the building direction (refer Fig. 5 (b) and Fig. 7 (b)). As such the plane stress approximation leads to an overestimation of the value of d_0 which results in calculating (slightly) compressive stresses along both directions Y and Z. Nevertheless, if directions Y or Z are assumed as "stress-free", the calculated residual stress magnitude does not exceed ±50 MPa, which appears to be the uncertainty of the stress calculation for these samples.

3.3. Annealed LPBF Alloy 718: calculated d_0 from plane stress assumption

The stresses in all the vertical and horizontal samples (measured using {311} lattice planes) were significantly relieved after the annealing treatment and the residual stress values are shown in Fig. 7 and Fig. 8. Sample #4 was chosen because of the lowest amount of stresses in the as-built condition, to further elucidate the significant effect of annealing treatment on the residual stresses. In Fig. 7 (a) for vertical sample, after the annealing treatment the residual stress profile flattened and was close to zero. In Fig. 7 (b), the stresses in *Z*-direction were observed to be compressive prior to the annealing treatment, while stress relaxation was observed after the annealing treatment. These results corroborate qualitatively with the observations of lattice spacing (d), as shown in Fig. 7 (c) and (d), which does not require plane stress assumption. Fig. 8 (a) and (b) show the residual stresses (along the Y and Z-directions) and Fig. 8 (c) and (d) show corresponding lattice spacings for the horizontal samples. In this case, too, similar stress relaxation was observed after annealing treatment as the vertical samples. The (slightly) tensile stress seen in Fig. 8 after annealing is considered negligible and it arises from the measurement inaccuracy and the plane stress assumption.

3.4. Residual stresses in as-built EB-PBF Alloy 718: using calculated d_0

The residual stress values in EB-PBF obtained from the {200} lattice planes for both vertical and horizontal samples are given in Fig. 9. On average, the stresses in the horizontally built specimens were similar to horizontally built LPBF material. However, for vertically oriented samples the stresses were much lower than in the LPBF process. The application of annealing treatment on EB-PBF samples had only minor effect on the residual stresses in the material.

4. Discussion

As mentioned in the experimental section, all the samples were removed from the base plates and previous studies have shown that this significantly affects the residual stress state of the material [14,18]. Kruth et al. [14] showed that tensile stresses exist in the LPBF material while attached to the build plate. After removing the material from the build plate, the stresses relax which can potentially lead to shrinkage and bending of the material. It is also worth mentioning that, at high temperatures encountered during processing, the yield strength is decreased which can cause plastic deformation due to thermal stresses, which in turn results in residual stresses as elaborated by Kruth et al. [14].

4.1. LPBF built Alloy 718

The findings in this work correlate well with already published results, that LPBF built Alloy 718 is prone to significant residual stresses [31,41]. The process parameters were found to influence the residual stress state of the as-built material. The various parameters which were systematically varied are stated in Table 2. It was observed that

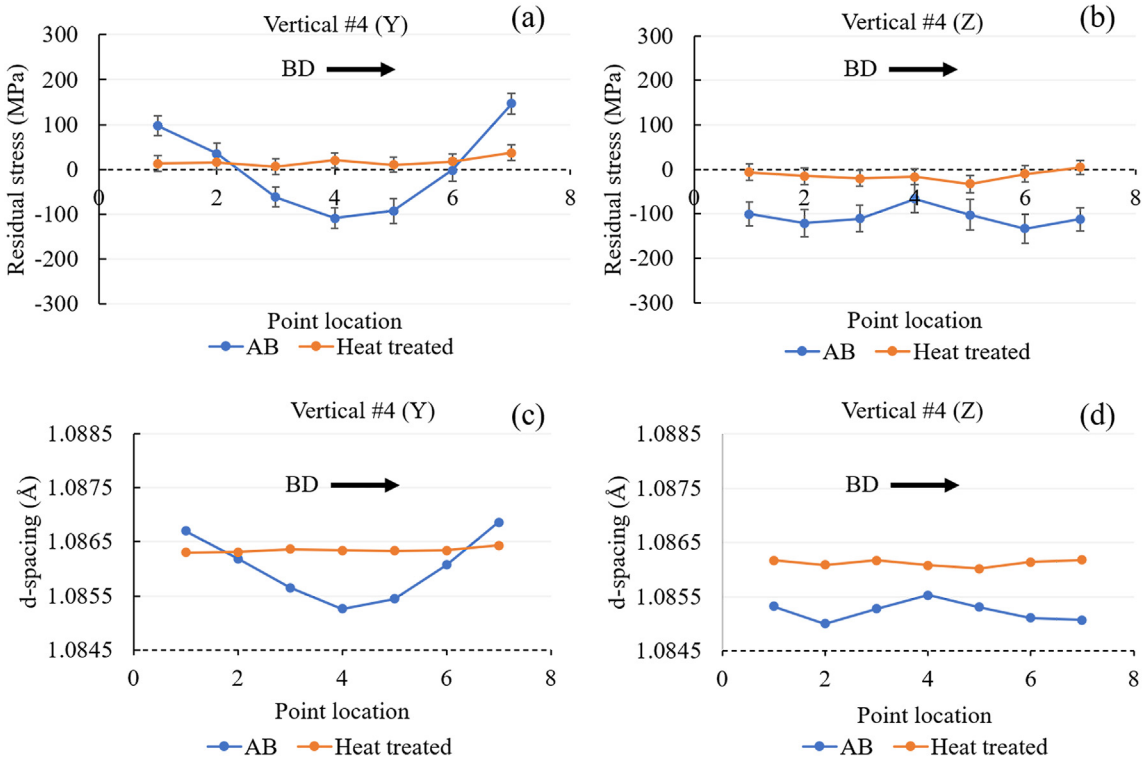

Fig. 7. Residual stresses along (a) Y and (b) Z in the vertical LPBF sample #4 before (AB) and after annealing treatment evaluated using Eqs. (3) and (4). The through thickness stress (along X) is assumed to be zero. The corresponding lattice spacing (d) of the {311} family of lattice planes in (c) Y and (d) Z directions. The arrow indicates the build direction.

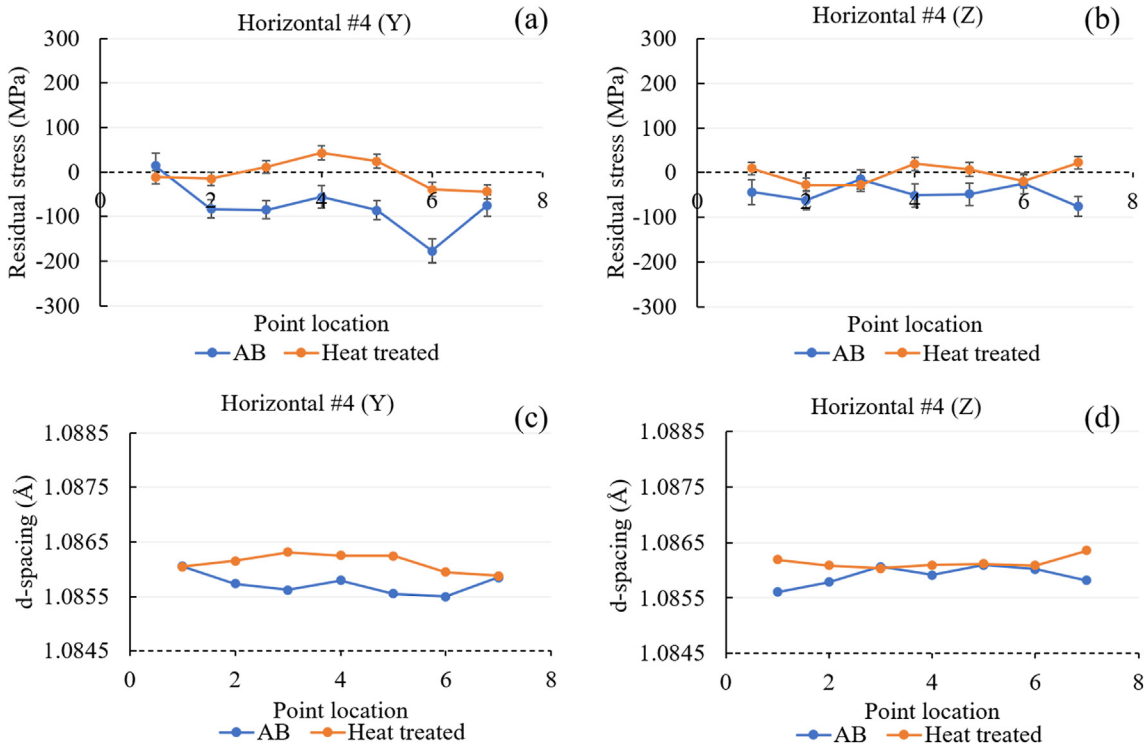

Fig. 8. Residual stresses along (a) Y and (b) Z in the horizontal LPBF sample #4 before (AB) and after annealing treatment evaluated using Eqs. (3) and (4). The through thickness stress (along X) is assumed to be zero. The corresponding lattice spacing (d) in (c) Y and (d) Z directions. All the points were measured at the same build height.

the hatching pattern influences the residual stresses, correlating well with the literature [16,18]. Lower amount of stress was observed for the vertical sample produced using chessboard strategy compared to the bi-directional raster scanning strategy (see Fig. 5), which has also been previously reported elsewhere [42]. The chessboard scan strategy is composed of squares of vectors, where neighboring squares have vectors aligned 67° with respect to each other. As it has been shown that the vectors are aligned with the residual stresses [16], it is possible that there is a superposition of the micro residual stresses, leading to a decreased macro residual stress level. The lower amount of residual stresses observed for chessboard strategy compared to raster strategy can also be explained by the more homogenous heating of the powder-bed in case of the former strategy, which would have reduced the thermal gradients thereby lowering the thermal residual stresses [43]. To gain further understanding of the effect of processing conditions, simulations can be performed, and the data from the present study can be used for calibrating such simulation models.

The magnitude of the residual stresses in the as-built material was dependent on the build orientation and height from the built plate. As shown in Fig. 5 (a), the residual stresses were tensile close to the build plate (point 1) and at the top (point 7) of the specimen, whereas they were compressive in the middle of the material. This too corresponds well with the findings of Mercelis et al. [18] as they had also similarly tested the samples after removal from the build plate. Kruth et al. [14] have explained this occurrence to be due to removal of the sample from the build plate, which changes the stress state in the material. There is a difference in the two graphs in Fig. 5 (a) and (b), in the Z direction the residual stresses are somewhat constant in nature- tensile or compressive (depending on the process parameters), while in Y direction they change from tensile to compressive to tensile. On the other hand, in horizontal sample, for stresses in Y direction, (Fig. 6 (a)), no U-shape (tensile-compressive-tensile) in the residual stress profile was observed, while in Z direction (Fig. 6 (b)) the trend is similar to in Fig. 5 (b), i.e., relatively constant stress level, though close to zero. The reason for this difference in vertical and horizontal sample (Y direction stresses) can be explained by the difference in the build orientation of the two investigated samples. For the horizontally built sample, the material is in contact with the build plate throughout the whole building time, corresponding to only the bottom point for the vertically built material, therefore this U-shape and stress variation linked to build plate offset cannot be observed. These stress variations could still be present throughout the thickness. However, due to limitations of the POLDI instrument, these could not be measured. Mercelis et al. [18] have also observed reduction in residual stress for lower build heights. It should be noted that the residual stresses do not appear to equilibrate, i.e. they do not seem to cancel each other as they all appear to be compressive. This is a result of the assumption that the stress is zero in the direction parallel to the wall thickness, which for this sample is parallel to the building direction along which typically the highest residual stresses are seen (see Fig. 5 (b)).

It was observed that the chessboard scanning strategy results in lower amount of residual stresses compared to the bi-directional raster scanning strategy. Further annealing treatment significantly reduced the residual stresses as shown in Fig. 7 and Fig. 8. The result of the annealing treatments corroborate well with Kruth et al.'s [14] observation for Ti-6Al-4V produced by LPBF.

4.2. EB-PBF compared with LPBF

Due to the strong crystallographic texture in EB-PBF samples, residual stresses were calculated using the {200} lattice planes, the results are shown in Fig. 9. When strongly textured materials are measured, the strong texture affects the intergranular microstrains accumulated during plastic deformation, which result in spurious residual lattice strains [44,45]. This makes the choice of diffraction peak particularly crucial for the correct characterization of residual strains. However, it was observed that the lattice strain variation along the 3 directions for the EB-PBF is negligible, thus negligible residual strains exist, and

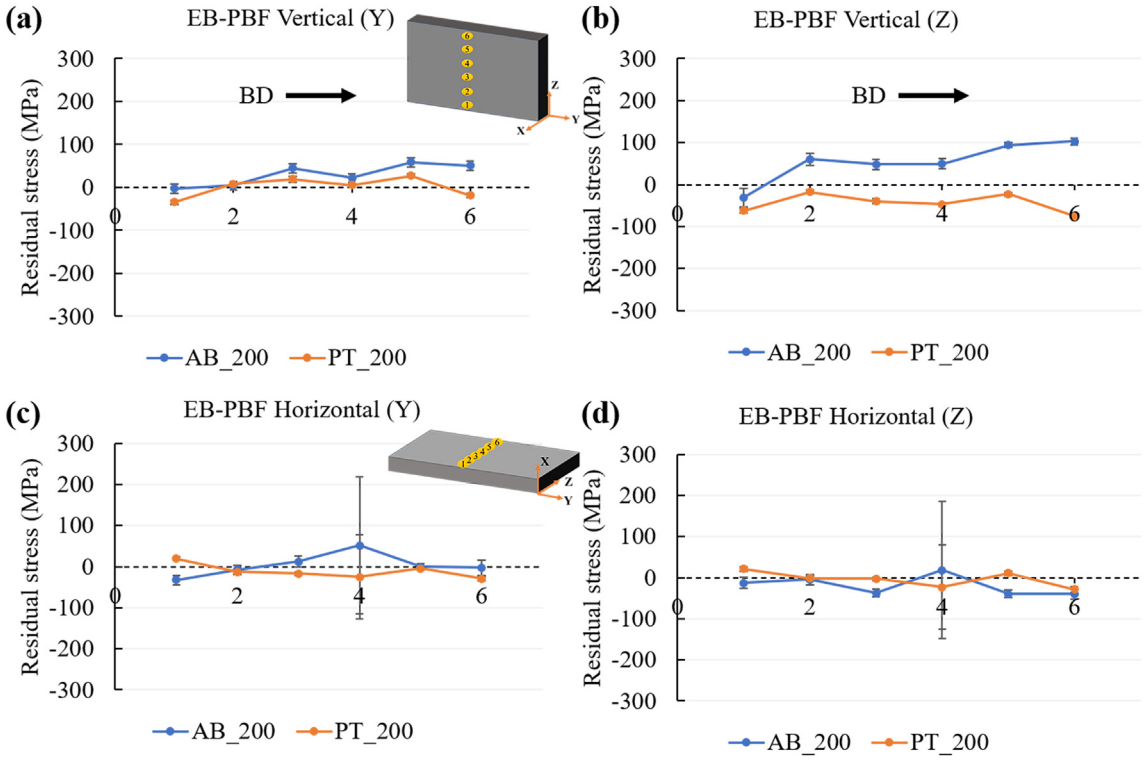

Fig. 9. Residual stresses along (a), (c) Y and (b), (c) Z directions in the EB-PBF samples before (AB) and after annealing treatment for (a), (b) vertical and (c), (d) horizontal samples using Eqs. (3) and (4). The through thickness stress (along X) is assumed to be zero. For vertical samples, the arrow indicates the build direction.

therefore the choice of {200} peak is not an issue. This is reasonable, because the residual stress values are lower than the yield strength of the material, even for LPBF (as typically reported in literature in the order of 1000 MPa [46]). Residual stress analyses based on the {200} and {311} peaks of the LPBF samples were in good agreement, within the experimental error. These observations are in good agreement with previous

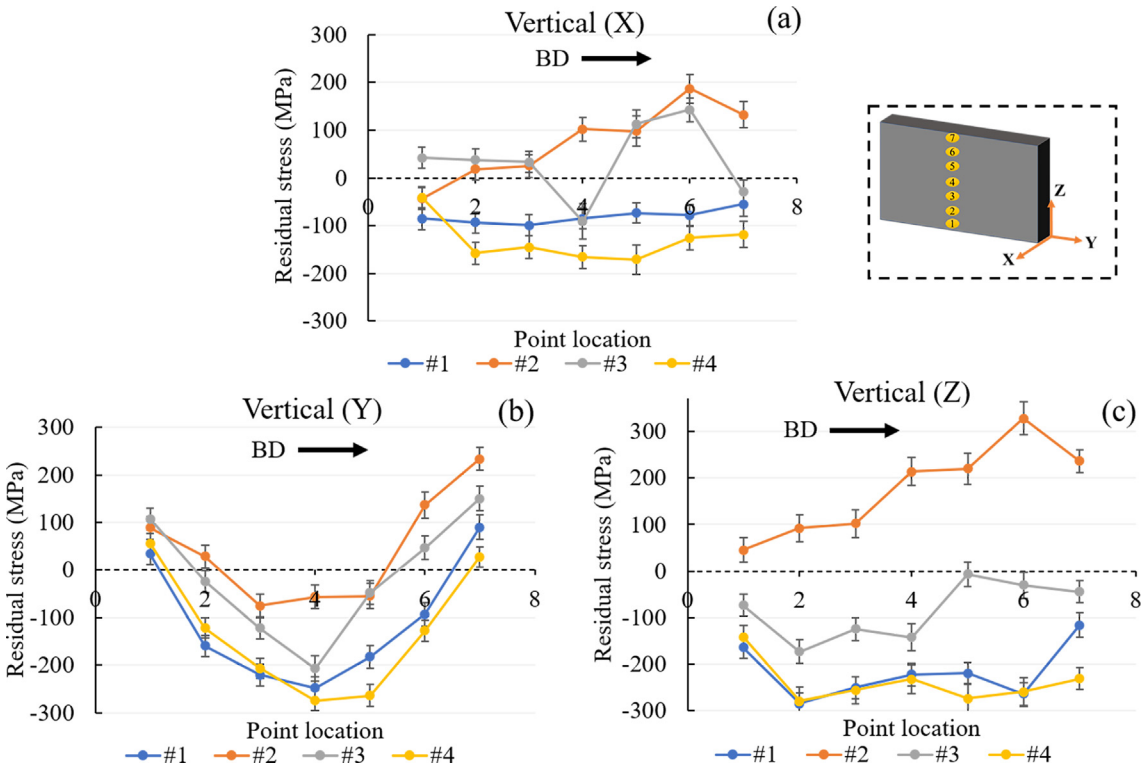

Fig. 10. Residual stress along (a) X, (b) Y and (c) Z directions for all the as-built LPBF vertical samples, using measured d_0 (Eqs. (1) and (2)). The arrow indicates the build direction.

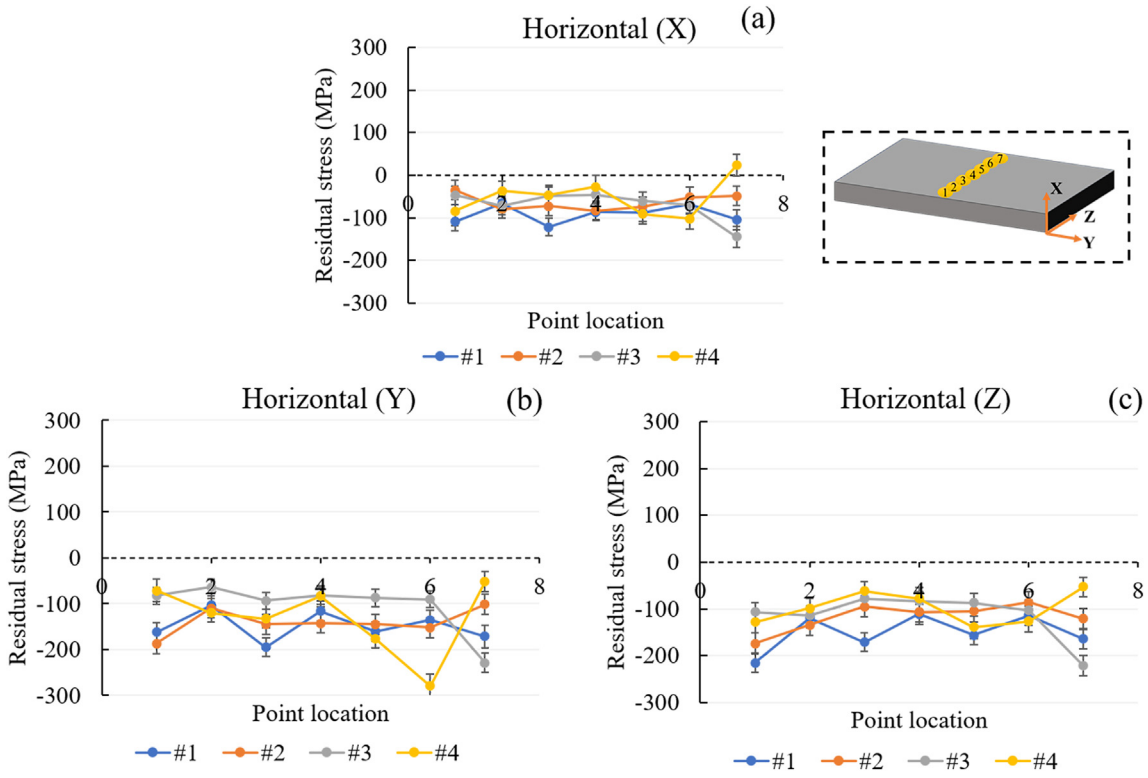

Fig. 11. Residual stress along (a) X, (b) Y and (c) Z directions for all the as-built LPBF horizontal samples, using measured d_0 (Eqs. (1) and (2)). All the points were measured at the same build height.

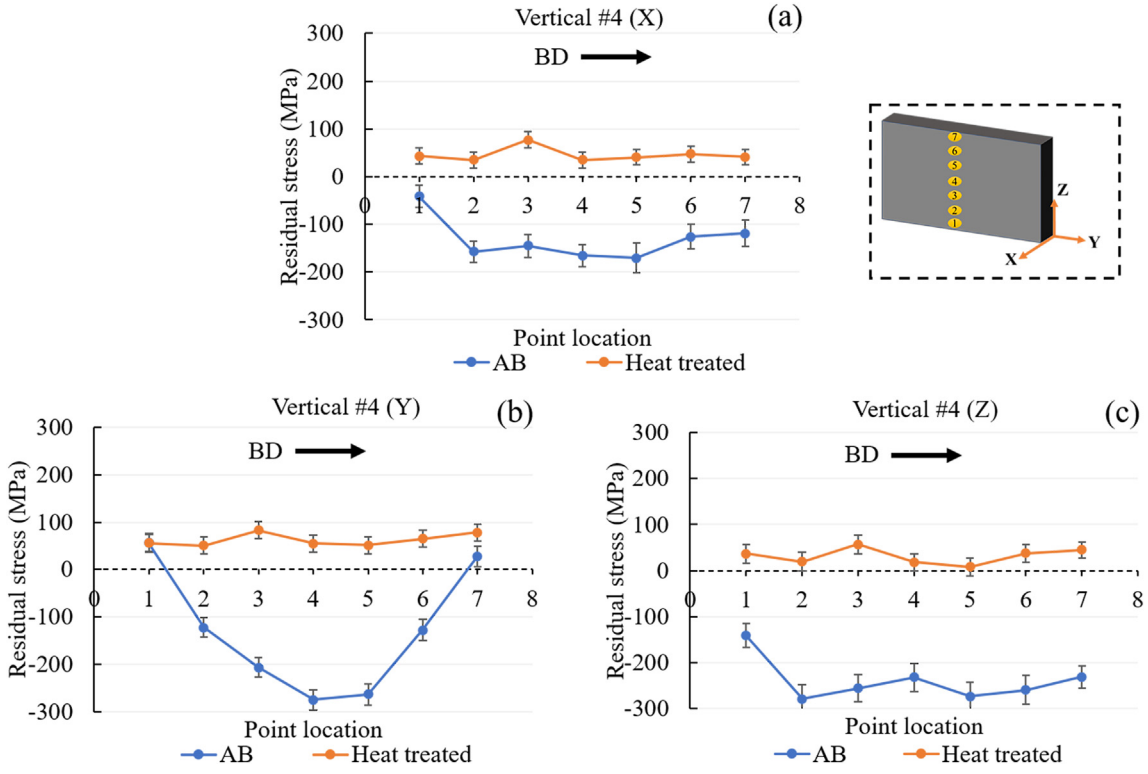

Fig. 12. Residual stress along (a) X, (b) Y and (c) Z directions in the vertical LPBF sample #4 before (AB) and after heat treatment, using measured d_0 (Eqs. (1) and (2)). The arrow indicates the build direction.

investigations on stainless steel (SS316L) manufactured by AM, where the stress values evaluated using neutron diffraction on {311} and {200} lattice planes were found to be in good agreement [28]. The results showing lower amount of residual stresses observed in EB-PBF samples compared to those by LPBF corroborate well with the previous work by Sochalski-Kolbus et al. [13]. The lower residual stress in EB-PBF sample can be explained by two factors: high powder-bed temperature and application of preheat step prior to melting. The applied high powder-bed temperature during EB-PBF process (~1000 °C) reduces the thermal gradient between the build plate and the layer being processed. Since residual stresses arise from temperature gradients, such processing conditions contribute to the reduction of residual stresses during EB-PBF, which is not the case during LPBF processing where steeper temperature gradients are expected [47].

4.3. Influence of d_0 on evaluation of residual stress in LPBF Alloy 718

One of the greatest concerns when determining residual stresses using diffraction-based measurements is the stress-free lattice spacing, d_0 [26]. Therefore, in the present study, d_0 was evaluated in two ways: (a) calculated d_0 by plane stress approximation, (b) measured d_0 using 'stress-free' reference sample. The results using the former approach are already discussed in Section 4.1, and those from the latter are given in Fig. 10 to Fig. 13, which were obtained using the 'stress-free' sample extracted from the annealed specimen shown in Fig. 3 (a). As shown in Fig. 11, all stress components for the as-built LPBF horizontal samples were compressive, which is not plausible in reality and, therefore, it can be inferred that this approach might be inaccurate and it implies that neither annealing nor the comb-type sectioning completely relieved the residual stresses. Moreover, the annealing treatment, prior to d_0 determination, was likely to have altered the chemical composition and consequently the d_0 value [48]. Since the annealing treatment was applied at 1066 °C for 2 h, it is expected to have led to significant, if not complete, dissolution of all the secondary phases, except carbides [49,50]. In addition, the application of quenching (1066 to 500 °C in ~5 min) after the hold time would have inhibited any considerable precipitation [51]. Therefore, the use of d_0 evaluated using plane stress approximation appears to be more appropriate in the present case because it gives reasonable results which corroborate with the existing literature, whereas those evaluated using the measured d_0 approach appears to overestimate the magnitude of residual stresses (see Fig. 5 vs. Fig. 10 and Fig. 6 vs. Fig. 11) while the annealed samples appear to contain residual stress (see Fig. 7 vs. Fig. 12 and Fig. 8 vs. Fig. 13), which is unexpected. Adopting the calculated d_0 approach also removes the need for stress-free references and accounts for the spatial variation in chemistry and microstructure. This accounts for any effect of compositional inhomogeneity on d-spacing and its consequent effects on calculated strains and thus stresses. Withers et al. [26] predict that local compositional changes in the alloy can have much larger influence on the lattice parameters in comparison to residual stress. It is noteworthy that, Rangaswamy et al. [28] studied a 5 mm thick stainless steel (SS316L) wall manufactured by AM and found through thickness stress, measured using neutron diffraction, to be negligible.

5. Conclusion

In this work, the residual stresses in Alloy 718 built using two powder bed fusion additive manufacturing processes, i.e., electron beam powder bed fusion (EB-PBF) and laser powder bed fusion (LPBF), have been analyzed. Both the influence of process parameters and thermal post-treatment on the residual stresses have been investigated using neutron diffraction. Neutron diffraction was found to be a convenient tool for measuring the residual stresses of additively manufactured materials, especially for non-destructive evaluation. Based on the experimental work the following conclusions could be drawn:

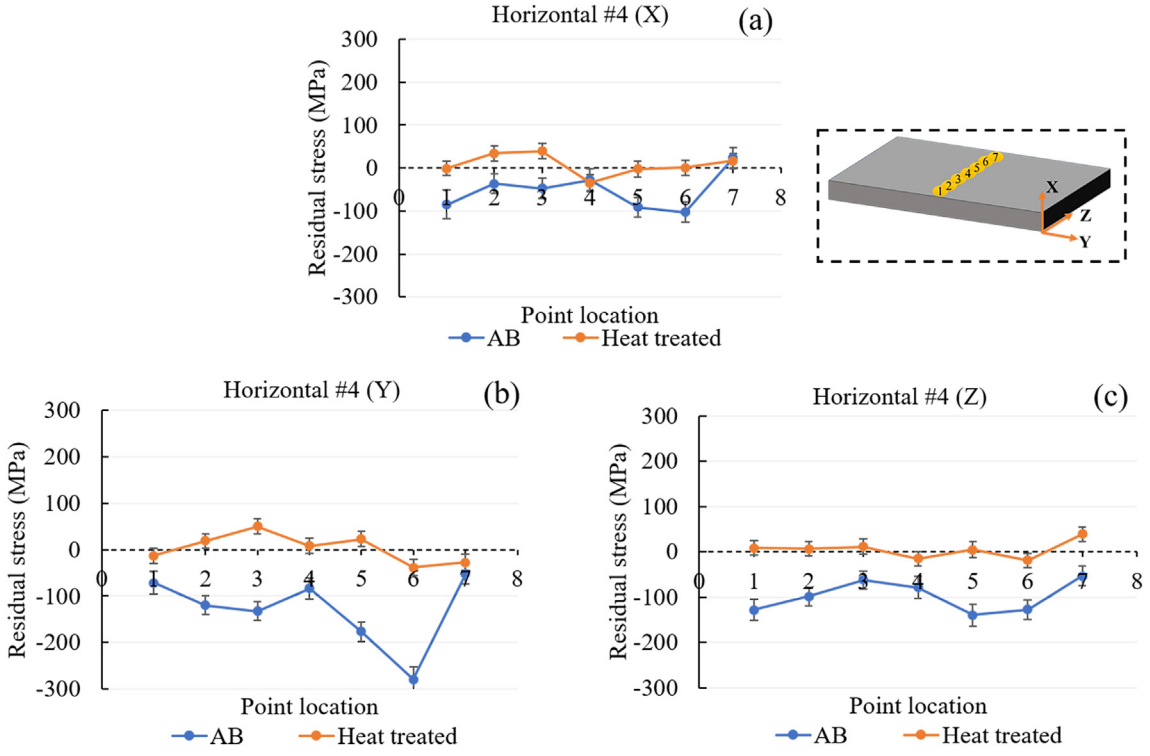

Fig. 13. Residual stress along (a) X, (b) Y and (c) Z directions in the horizontal LPBF sample #4 before (AB) and after heat treatment, using measured d_0 (Eqs. (1) and (2)). All the points were measured at the same build height.

- In as-built condition, chessboard scanning pattern compared to bi-directional raster scanning resulted in lower amount of residual stresses in the material.
- Vertically built material showed presence of a tensile-compression-tensile stress gradient in the material, whereas stresses in horizontally built material were relatively constant and lower in amount.
- Heat treatments at 1066 °C for 2 h greatly reduced the residual stresses in the material.
- Significantly lower residual stresses were found in as-built EB-PBF material, compared to the LPBF, which is attributed to the lower temperature gradient in the former.
- The measured d_0 was significantly influenced by how the stress-free reference sample was produced, i.e. how the comb-type cuts relax stress or if annealing introduces chemical variations.
- Unlike measured d_0, calculated d_0 assumes a plane stress condition, gives reasonable results for thin-walled samples, however, it might not be valid for thick material.

Data availability

The raw/processed data required to reproduce these findings cannot be shared at this time due to technical or time limitations.

Declaration of Competing Interest

The authors declare that they have no known competing financial interests or personal relationships that could have appeared to influence the work reported in this paper.

Acknowledgement

The authors would like to thank GKN Aerospace Sweden AB for providing the material used within this work. Thanks to Sandvik Additive Manufacturing for providing the powder for EB-PBF build. Furthermore, Paul Sherrer Institute is acknowledged for providing the beamline time required for this experimental work to be conducted. Thanks to Mr. Nitesh Raj Jaladugram (Chalmers University of Technology, Sweden) and Mr. Arun Ramanathan Balachandramurthi (University West, Sweden) for assistance during the neutron diffraction experiments. This work was supported by the KK Foundation, Sweden [grant number 20160281], and SpaceLab Project. Further funding from the European Union's Horizon 2020 research and innovation program under the Marie Skłodowska-Curie grant agreement No. 701647 is also acknowledged.

References

[1] R.C. Reed, The physical metallurgy of nickel and its alloys, Superalloys Fundam. Appl, Cambridge University Press, Cambridge, 2006.
[2] D. Fournier, A. Pineau, Low cycle fatigue behavior of Inconel 718 at 298 K and 823 K, Metall. Trans. A. 8A (1977) 1095–1105, https://doi.org/10.1007/BF02667395.
[3] I. Gibson, D. Rosen, B. Stucker, Additive manufacturing technologies, 1st ed. Springer, New York, 2010.
[4] M. Neikter, Microstructure and hydrogen embrittlement of additively manufactured Ti-6Al-4V, Luleå University of Technology, 2019 PhD Thesis.
[5] B. Dutta, F.H. (Sam) Froes, The Additive Manufacturing (AM) of titanium alloys, Met. Powder Rep. 72 (2017) 96–106, https://doi.org/10.1016/j.mprp.2016.12.062.
[6] W.E. Frazier, Metal additive manufacturing: a review, J. Mater. Eng. Perform. 23 (2014) 1917–1928, https://doi.org/10.1007/s11665-014-0958-z.
[7] M. Neikter, F. Forsberg, R. Pederson, M.-L. Antti, P. Åkerfeldt, S. Larsson, P. Jonsén, G. Puyoo, Defect characterization of electron beam melted Ti-6Al-4V and Alloy 718 with X-ray microtomography, Aeronaut. Aerosp. Open Access J. 2 (2018) 139–145, https://doi.org/10.15406/aaoaj.2018.02.00044.
[8] M. Neikter, A. Huang, X. Wu, Microstructural characterization of binary microstructure pattern in selective laser-melted Ti-6Al-4V, Int. J. Adv. Manuf. Technol. 104 (2019) 1381–1391, https://doi.org/10.1007/s00170-019-04002-8.
[9] L.L. Parimi, D. Clark, M.M. Attallah, Microstructural and texture development in direct laser fabricated IN718, Mater. Charact. 89 (2014) 102–111, https://doi.org/10.1016/j.matchar.2013.12.012.
[10] M. Neikter, R. Woracek, T. Maimaitiyili, C. Scheffzük, M. Strobl, M.L. Antti, P. Åkerfeldt, R. Pederson, C. Bjerkén, Alpha texture variations in additive manufactured Ti-6Al-4V investigated with neutron diffraction, Addit. Manuf. 23 (2018) 225–234, https://doi.org/10.1016/j.addma.2018.08.018.
[11] T. Maimaitiyili, R. Woracek, M. Neikter, M. Boin, R.C. Wimpory, R. Pederson, M. Strobl, M. Drakopoulos, N. Schäfer, C. Bjerkén, Residual lattice strain and phase distribution in Ti-6Al-4V produced by electron beam melting, Materials (Basel) 12 (2019) 667, https://doi.org/10.3390/ma12040667.
[12] T. Thiede, S. Cabeza, T. Mishurova, N. Nadammal, A. Kromm, J. Bode, C. Haberland, G. Bruno, Residual stress in selective laser melted Inconel 718: influence of the removal from base plate and deposition hatch length, Mater. Perform. Charact. 7 (2018) 717–735, https://doi.org/10.1520/MPC20170119.
[13] L.M. Sochalski-Kolbus, E.A. Payzant, P.A. Cornwell, T.R. Watkins, S.S. Babu, R.R. Dehoff, M. Lorenz, O. Ovchinnikova, C. Duty, Comparison of residual stresses in Inconel 718 simple parts made by electron beam melting and direct laser metal sintering, Metall. Mater. Trans. A 46 (2015) 1419–1432, https://doi.org/10.1007/s11661-014-2722-2.
[14] J.-P. Kruth, J. Deckers, E. Yasa, R. Wauthlé, Assessing and comparing influencing factors of residual stresses in selective laser melting using a novel analysis method, J. Eng. Manuf. 226 (2012) 980–991, https://doi.org/10.1177/0954405412437085.
[15] M.M. Attallah, R. Jennings, X. Wang, L.N. Carter, Additive manufacturing of Ni-based superalloys: the outstanding issues, MRS Bull. 41 (2016) 758–764, https://doi.org/10.1557/mrs.2016.211.
[16] J. Robinson, I. Ashton, P. Fox, E. Jones, C. Sutcliffe, Determination of the effect of scan strategy on residual stress in laser powder bed fusion additive manufacturing, Addit. Manuf. 23 (2018) 13–24, https://doi.org/10.1016/j.addma.2018.07.001.
[17] H. Ali, H. Ghadbeigi, K. Mumtaz, Effect of scanning strategies on residual stress and mechanical properties of selective laser melted Ti6Al4V, Mater. Sci. Eng. A 712 (2018) 175–187, https://doi.org/10.1016/j.msea.2017.11.103.
[18] P. Mercelis, J.J.-P. Kruth, Residual stresses in selective laser sintering and selective laser melting, Rapid Prototyp. J. 12 (2006) 254–265, https://doi.org/10.1108/13552540610707013.
[19] L. Parry, I.A. Ashcroft, R.D. Wildman, Understanding the effect of laser scan strategy on residual stress in selective laser melting through thermo-mechanical simulation, Addit. Manuf. 12 (2016) 1–15, https://doi.org/10.1016/j.addma.2016.05.014.
[20] T. Vilaro, C. Colin, J.D. Bartout, L. Nazé, M. Sennour, Microstructural and mechanical approaches of the selective laser melting process applied to a nickel-base superalloy, Mater. Sci. Eng. A 534 (2012) 446–451, https://doi.org/10.1016/j.msea.2011.11.092.
[21] M.E. Fitzpatrick, A. Lodini, Analysis of Residual Stress by Diffraction Using Neutron and Synchrotron Radiation, Taylor & Francis, 2003.
[22] V. Hauk, H. Behnken, Structural and residual stress analysis by nondestructive methods : evaluation, application, assessment, Elsevier, 1997.
[23] P.J. Withers, H.K.D.H. Bhadeshia, Residual stress part 1 - measurement techniques, Mater. Sci. Technol. 17 (2001) 355–365, https://doi.org/10.1179/026708301101509980.
[24] P.J. Withers, H.K.D.H. Bhadeshia, Residual stress part 2 - nature and origins, Mater. Sci. Technol. 17 (2001) 366–375, https://doi.org/10.1179/026708301101510087.
[25] U.F. Kocks, C.N. Tomé, H.-R. Wenk, Texture and anisotropy: preferred orientations in polycrystals and their effect on materials properties, Cambridge University Press, Cambridge, 1998.
[26] P.J. Withers, M. Preuss, A. Steuwer, J.W.L. Pang, Methods for obtaining the strain-free lattice parameter when using diffraction to determine residual stress, J. Appl. Crystallogr. 40 (2007) 891–904, https://doi.org/10.1107/S0021889807030269.
[27] K. An, L. Yuan, L. Dial, I. Spinelli, A.D. Stoica, Y. Gao, Neutron residual stress measurement and numerical modeling in a curved thin-walled structure by laser powder bed fusion additive manufacturing, Mater. Des. 135 (2017) 122–132, https://doi.org/10.1016/j.matdes.2017.09.018.
[28] P. Rangaswamy, M.L. Griffith, M.B. Prime, T.M. Holden, R.B. Rogge, J.M. Edwards, R.J. Sebring, Residual stresses in LENS® components using neutron diffraction and contour method, Mater. Sci. Eng. A 399 (2005) 72–83, https://doi.org/10.1016/j.msea.2005.02.019.
[29] P.J. Withers, P.J. Webster, Neutron and synchrotron X-ray strain scanning, Strain 37 (2001) 19–33, https://doi.org/10.1111/j.1475-1305.2001.tb01216.x.
[30] Y. Lu, S. Wu, Y. Gan, T. Huang, C. Yang, L. Junjie, J. Lin, Study on the microstructure, mechanical property and residual stress of SLM Inconel-718 alloy manufactured by differing island scanning strategy, Opt. Laser Technol. 75 (2015) 197–206, https://doi.org/10.1016/j.optlastec.2015.07.009.
[31] T. Mishurova, S. Cabeza, T. Thiede, N. Nadammal, A. Kromm, M. Klaus, C. Genzel, C. Haberland, G. Bruno, The influence of the support structure on residual stress and distortion in SLM Inconel 718 parts, Metall. Mater. Trans. A 49 (2018) 3038–3046, https://doi.org/10.1007/s11661-018-4653-9.
[32] S. Goel, A. Sittiho, I. Charit, U. Klement, S. Joshi, Effect of post-treatments under hot isostatic pressure on microstructural characteristics of EBM-built Alloy 718, Addit. Manuf. 28 (2019) 727–737, https://doi.org/10.1016/j.addma.2019.06.002.
[33] Z. Wang, E. Denlinger, P. Michaleris, A.D. Stoica, D. Ma, A.M. Beese, Residual stress mapping in Inconel 625 fabricated through additive manufacturing: method for neutron diffraction measurements to validate thermomechanical model predictions, Mater. Des. 113 (2017) 169–177, https://doi.org/10.1016/j.matdes.2016.10.003.
[34] W. Woo, Z. Feng, X.-L. Wang, S.A. David, Neutron diffraction measurements of residual stresses in friction stir welding: a review, Sci. Technol. Weld. Join. 16 (2011) 23–32, https://doi.org/10.1179/136217110X12731414739916.
[35] ISO, ISO 21432:2019 - Non-Destructive Testing — Standard test Method for Determining Residual Stresses by Neutron Diffraction, 2019.
[36] O. Arnold, J.C. Bilheux, J.M. Borreguero, A. Buts, S.I. Campbell, L. Chapon, M. Doucet, N. Draper, R. Ferraz Leal, M.A. Gigg, V.E. Lynch, A. Markvardsen, D.J. Mikkelson, R.L. Mikkelson, R. Miller, K. Palmen, P. Parker, G. Passos, T.G. Perring, P.F. Peterson, S. Ren, M.A. Reuter, A.T. Savici, J.W. Taylor, R.J. Taylor, R. Tolchenov, W. Zhou, J.

Zikovsky, Mantid-Data analysis and visualization package for neutron scattering and μ SR experiments, Nucl. Instruments Methods Phys. Res. A 764 (2014) 156–166, https://doi.org/10.1016/j.nima.2014.07.029.
[37] X. Huang, M.C. Chaturvedi, N.L. Richards, Effect of homogenization heat treatment on the microstructure and heat-affected zone microfissuring in welded cast Alloy 718, Metall. Mater. Trans. A 27A (1996) 785–790, https://doi.org/10.1007/BF02648966.
[38] J. Schneider, B. Lund, M. Fullen, Effect of heat treatment variations on the mechanical properties of Inconel 718 selective laser melted specimens, Addit. Manuf. 21 (2018) 248–254, https://doi.org/10.1016/j.addma.2018.03.005.
[39] P.E. Aba-Perea, T. Pirling, P.J. Withers, J. Kelleher, S. Kabra, M. Preuss, Determination of the high temperature elastic properties and diffraction elastic constants of Ni-base superalloys, Mater. Des. 89 (2016) 856–863, https://doi.org/10.1016/j.matdes.2015.09.152.
[40] Y. Wang, J. Shi, Y. Liu, Competitive grain growth and dendrite morphology evolution in selective laser melting of Inconel 718 superalloy, J. Cryst. Growth 521 (2019) 15–29, https://doi.org/10.1016/j.jcrysgro.2019.05.027.
[41] Y. Lu, S. Wu, Y. Gan, T. Huang, C. Yang, L. Junjie, J. Lin, Study on the microstructure, mechanical property and residual stress of SLM Inconel-718 alloy manufactured by differing island scanning strategy, Opt. Laser Technol. 75 (2015) 197–206, https://doi.org/10.1016/j.optlastec.2015.07.009.
[42] J.P. Kruth, L. Froyen, J. Van Vaerenbergh, P. Mercelis, M. Rombouts, B. Lauwers, Selective laser melting of iron-based powder, J. Mater. Process. Technol 2004, pp. 616–622, https://doi.org/10.1016/j.jmatprotec.2003.11.051.
[43] L. Mugwagwa, D. Dimitrov, S. Matope, I. Yadroitsev, Evaluation of the impact of scanning strategies on residual stresses in selective laser melting, Int. J. Adv. Manuf. Technol. 102 (2019) 2441–2450, https://doi.org/10.1007/s00170-019-03396-9.
[44] J. Repper, P. Link, M. Hofmann, C. Krempaszky, W. Petry, E. Werner, Interphase microstress measurements in IN718 by cold neutron diffraction, Appl. Phys. A Mater. Sci. Process. 99 (2010) 565–569, https://doi.org/10.1007/s00339-010-5607-2.
[45] J.N. Wagner, M. Hofmann, S. Van Petegem, C. Krempaszky, M. Hoelzel, M. Stockinger, Comparison of intergranular strain formation of conventional and newly developed nickel based superalloys, Mater. Sci. Eng. A 662 (2016) 303–307, https://doi.org/10.1016/j.msea.2016.03.059.
[46] M.M. Kirka, K.A. Unocic, N. Raghavan, F. Medina, R.R. Dehoff, S.S. Babu, Microstructure development in electron beam-melted Inconel 718 and associated tensile properties, JOM. 68 (2016) 1012–1020, https://doi.org/10.1007/s11837-016-1812-6.
[47] X. Zhao, S. Li, M. Zhang, Y. Liu, T.B. Sercombe, S. Wang, Y. Hao, R. Yang, L.E. Murr, Comparison of the microstructures and mechanical properties of Ti-6Al-4V fabricated by selective laser melting and electron beam melting, Mater. Des. 95 (2016) 21–31, https://doi.org/10.1016/j.matdes.2015.12.135.
[48] R.Y. Zhang, H.L. Qin, Z.N. Bi, J. Li, S. Paul, T.L. Lee, S.Y. Zhang, J. Zhang, H.B. Dong, Evolution of lattice spacing of gamma double prime precipitates during aging of polycrystalline Ni-Base superalloys: an in situ investigation, Metall. Mater. Trans. A 51A (2020) 574–585, https://doi.org/10.1007/s11661-019-05536-y.
[49] M.E. Aydinöz, F. Brenne, M. Schaper, C. Schaak, W. Tillmann, J. Nellesen, T. Niendorf, On the microstructural and mechanical properties of post-treated additively manufactured Inconel 718 superalloy under quasi-static and cyclic loading, Mater. Sci. Eng. A 669 (2016) 246–258, https://doi.org/10.1016/j.msea.2016.05.089.
[50] V.A. Popovich, E.V. Borisov, A.A. Popovich, V.S. Sufiiarov, D.V. Masaylo, L. Alzina, Impact of heat treatment on mechanical behaviour of Inconel 718 processed with tailored microstructure by selective laser melting, Mater. Des. 131 (2017) 12–22, https://doi.org/10.1016/j.matdes.2017.05.065.
[51] L. Geng, Y.-S. Na, N.-K. Park, Continuous cooling transformation behavior of Alloy 718, Mater. Lett. 30 (1997) 401–405, https://doi.org/10.1016/S0167-577X(96)00225-X.